

# Imaging igneous rocks on the North Atlantic rifted continental margin

A. W. Roberts,<sup>1\*</sup> R. S. White<sup>1</sup> and P. A. F. Christie<sup>2</sup>

<sup>1</sup>*Bullard Laboratories, Madingley Rise, Madingley Road, Cambridge CB3 0EZ, UK. E-mail: a.w.roberts@dur.ac.uk*

<sup>2</sup>*Schlumberger Cambridge Research, High Cross, Madingley Road, Cambridge CB3 0EL, UK*

Accepted 2009 June 21. Received 2009 June 19; in original form 2008 November 20

## SUMMARY

Extruded basalt flows with thicknesses of several kilometres occur ubiquitously along the rifted continental margins of the northern North Atlantic. Their total volume exceeds 1 million km<sup>3</sup>, and may reach several million cubic kilometres. Intruded igneous rock comprising the complementary melt fraction to that extruded at the surface should exist in the lower crust with a volume at least as large as that of the extrusive basalts. To image the extrusive and intrusive igneous rocks on the continental margin near the Faroe Islands, in 2002 we shot a 375 km long deep-penetration seismic profile across the margin using 85 ocean bottom seismometers for wide-angle acquisition and shot a separate reflection profile using a 12 km streamer for optimal imaging. By using large airgun sources tuned to produce low frequency energy we were able to constrain the seismic velocity structure of the whole crust. We imaged not only layering and structure within the extrusive basalts, but also lower-crustal intrusions on the continent–ocean transition (COT). Combination of good velocity control on the lower-crust together with direct imaging of the extrusive basalts enables us to constrain the volumes of extrusive and intrusive igneous rocks produced near the Faroe Islands to be 340–420 and 560–780 km<sup>3</sup> per kilometre along strike, respectively. The COT marked both by high-velocity intrusions and lower-crustal layering is surprisingly narrow, with only 50 km separating unstretched continental crust from fully oceanic crust. In contrast, the extruded basalts flow up to 150 km landward at the paleo-surface.

**Key words:** Controlled source seismology; Seismic tomography; Continental margins: divergent; Crustal structure; Atlantic Ocean; Europe.

## 1 INTRODUCTION

The northern North Atlantic margins are characterized by large volumes of extruded volcanic rocks (Larsen & Jakobsdóttir 1988; White & McKenzie 1989; Stoker *et al.* 1993; Coffin & Eldholm 1994; Eldholm & Grue 1994; Holbrook *et al.* 2001; Sørensen 2003) reaching more than 1 million km<sup>3</sup> in total volume. Volcanic flows have been imaged on many seismic reflection profiles in the area (Larsen & Jakobsdóttir 1988; Flidner & White 2001b; White *et al.* 2003), whereas the presence of underplated or lower-crustal intruded igneous sections have been inferred from seismic velocities measured from wide-angle seismic profiles (Kodaira *et al.* 1995; Holbrook *et al.* 2001; Hopper *et al.* 2003; White *et al.* 2008).

The major period of basalt eruption was around the time of Tertiary continental breakup (Abrahamsen *et al.* 1984; Waagstein 1988; Sørensen 2003), and occurred in two main phases near 62

and 55 Ma. The basalt sequences are typically around 3 km in thickness, although they may reach more than 5 km in places, particularly under the Faroe Islands (White *et al.* 2003; Christie *et al.* 2006; Spitzer *et al.* 2008). At the continental margin, clear seaward-dipping reflector (SDR) sequences are imaged on reflection profiles, representing the location of continental extension and eventual rupture. These sequences are caused by repeated cycles of subaerial basalt extrusion and crustal subsidence (thermal and extensional) as continental rifting proceeded to breakup. Pálmason (1980), Hinz (1981) and Spitzer *et al.* (2005) discuss their generation and the imaging of SDR sequences in detail.

Richardson *et al.* (1999), using data from the Faroes Large Aperture Research Experiment (FLARE) and the Faroe-Shetland Traverse (FAST) profiles, show basalt flows overlying a lower velocity layer (presumed late Mesozoic or Paleocene sediment) on the Faroes shelf. Like the earlier work of Mudge & Rashid (1987), Richardson *et al.* (1999) also showed the presence of tilted, rotated fault blocks in the southern part of the Faroe-Shetland Basin, outside the region of basalt cover. It is presumed, although due to the difficulties in imaging through heterogeneous basalt structures it has not been

\*Current address: Department of Earth Sciences, Durham University, Science Laboratories, Durham DH1 3LE, UK.

directly observed, that these fault blocks extend under the basalt onto the northern slope of the Faroe-Shetland Basin. The velocities of the underlying sediment layer determined by Richardson *et al.* (1999) were, however, not well constrained due to a trade-off between velocity and thickness during modelling of the wide-angle seismic arrivals.

Petrological arguments suggest that extruded basalts at a continental margin should be accompanied by high velocity igneous material ponded at the base of, or intruded into the lower continental crust as sills (Cox 1980). An indicator of the composition of intrusive rocks, and thus of the temperature of the mantle from which they were formed, is seismic velocity; higher velocity rocks containing a greater MgO fraction are indicative of formation from mantle at a higher temperature (White & McKenzie 1989; Korenaga *et al.* 2000). High velocity material at the continent–ocean transition (COT) has been reported from several surveys on the North Atlantic margins. At Hatton Bank, Fowler *et al.* (1989) observed lower-crustal velocities of  $7.3\text{--}7.4\text{ km s}^{-1}$  at the COT, whereas a more detailed profile in the same region found velocities up to  $7.4\text{ km s}^{-1}$  (White *et al.* 2008; White & Smith 2009). Further south, at Edoras Bank, Barton & White (1997) found a thinner high-velocity wedge in the lower-crust with velocities up to  $7.5\text{ km s}^{-1}$ . To the north, on the Møre margin, Breivik *et al.* (2006) report velocities up to  $7.1\text{--}7.2\text{ km s}^{-1}$  at the COT. Vogt *et al.* (1998), Korenaga *et al.* (2002), Hopper *et al.* (2003), Klingelhöfer *et al.* (2005) and Voss & Jokat (2007) have also observed similar velocities in the deep COT crust at other locations in the North Atlantic. Beneath Iceland, Staples *et al.* (1997) found velocities of up to  $7.35\text{ km s}^{-1}$  in very young crust formed in the rift zone. On the western side of the Atlantic, Korenaga *et al.* (2000), Holbrook *et al.* (2001) and Hopper *et al.* (2003) have published work constraining the velocity field of the east Greenland margin (including a profile almost conjugate to the Hatton Bank margin), and overlaid onto it a 3 km streamer profile, allowing for joint interpretation of the stratigraphy and velocity field. They found velocities of up to  $7.5\text{ km s}^{-1}$  along the profile conjugate to the Hatton Bank profile of White & Smith (2009). Their streamer data, however, did not image the deep crust, so although the velocity field at depth was constrained by the wide-angle data set, it was not possible for them to jointly interpret the reflection and refraction data to control the deep COT structure.

## 2 DATA ACQUISITION

In summer 2002, two collinear 2-D seismic surveys, one using a multichannel seismic system and the other a wide-angle survey employing 85 four-component ocean bottom seismometers (OBS), were acquired near to the Faroe Islands. The 375 km profile reported here stretches from  $60.8^\circ\text{N } 2.8^\circ\text{W}$ , west of the Shetland Islands, across the Faroe-Shetland Basin and the Fugloy Ridge, finishing over oceanic crust at  $64.0^\circ\text{N } 5.2^\circ\text{W}$ , north of the Faroe Islands (Fig. 1).

### 2.1 Multichannel seismic acquisition

For the first survey, the WesternGeco vessel *Geco Topaz* shot a 167 litre ( $10\,170\text{ in}^3$ ) low frequency airgun source towed at 18 m depth (Lunnon *et al.* 2003) every 50 m into three, parallel streamers, with active lengths of 4, 12 and 4 km. The streamers were acoustically cross-braced and had sensors at 3.125 m intervals. The data from each individual sensor were recorded, so that the data could be digitally group-formed as the first step of processing.

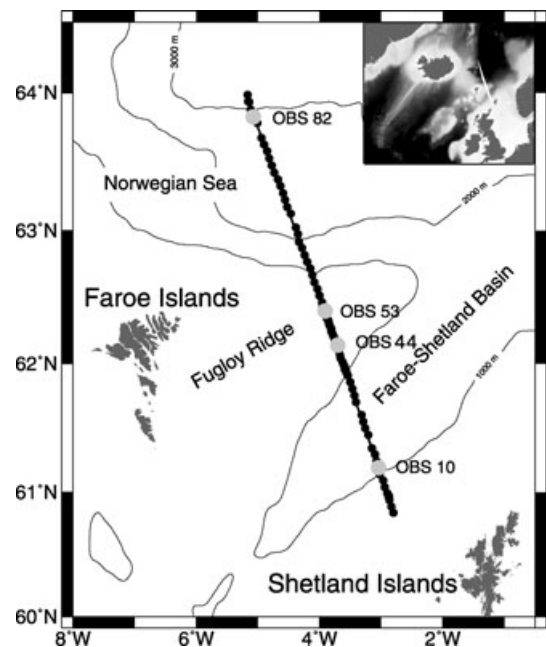


**Figure 1.** Location of the iSIMM Faroes line (thin line) and OBS positions (filled circles). OBS 10, 53 and 82, from which the data in Fig. 2 are taken, are marked with large circles, as is OBS 44, data from which are shown in Figs 4 and 10.

### 2.2 Wide-angle OBS data acquisition

The second survey used the *RRS Discovery* which deployed 85 OBS along the same line as the MCS (multichannel seismic) survey. The normal seismometer spacing was 6 km but over the Fugloy Ridge, a region of thick basalt cover, the spacing was reduced to 2 km (Fig. 1). A deep-towed 104 litre ( $6,340\text{ in}^3$ ) low frequency airgun source (Lunnon *et al.* 2003) was fired every 100 m along the profile into the seismometer array. The basalt structures that dominate the upper crust in this region pose a particular challenge to seismic imaging (Maresh & White 2005; Christie *et al.* 2006; Maresh *et al.* 2006). The reason for this is that although the intrinsic basaltic quality factor ( $Q$ ) is large, frequencies above about 20 Hz are severely attenuated due to the fact that the basalt sequences do not form a smooth homogeneous block, but rather a heterogeneous assemblage of layers and blocks, which vary on scales of metres to hundreds of metres. Maresh & White (2005) and Maresh *et al.* (2006) show from forward modelling that this attenuation can be described by an effective  $Q$  value of 20–40, similar to those measured in a borehole through Tertiary basalts in Rockall Trough, whereas Shaw *et al.* (2008) confirm low effective  $Q$  values from borehole measurements in the Faroe Islands. The seismic source and other acquisition parameters for this survey were designed to produce low-frequency energy to maximize the penetration of the seismic energy through the heterogeneous basalt structures which are characteristic of this region, building on the work of Ziolkowski *et al.* (2001) and others.

With 96 percent data recovery, the OBS data set was of high quality (Fig. 2), with wide-angle Moho reflections visible up to 150 km from the source. Due to ocean currents, the seismometer deployment positions were not directly above the points at which the seismometers landed on the seabed. By using the bathymetry data from an onboard echo sounder and the water wave arrival times, it was possible to calculate how far from the intended 2-D line each OBS had landed, and it was found that some had drifted up to 500 m from the line. To be able to model the profile as a 2-D line, time

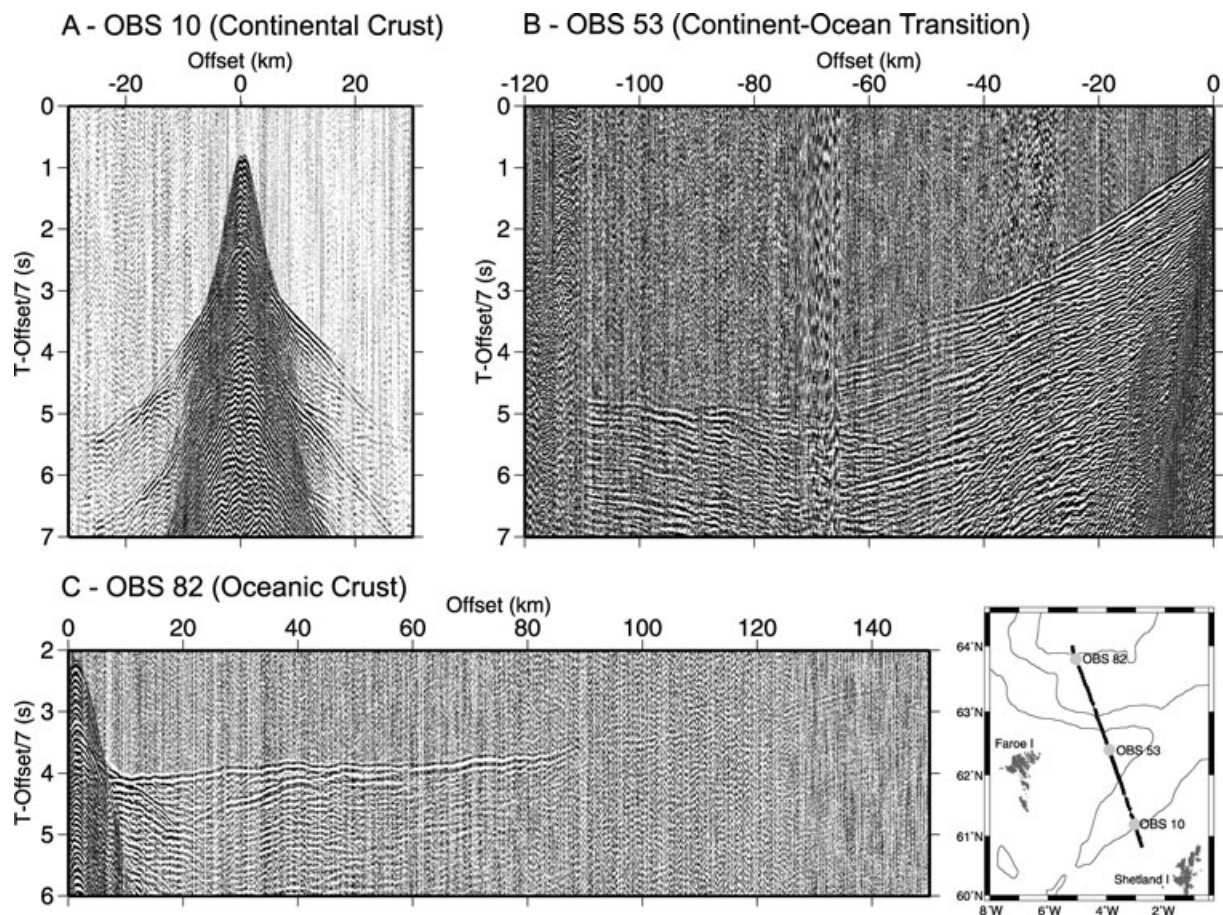


**Figure 2.** Examples of data from (A) OBS 10 (Faroe-Shetland Basin), (B) OBS 53 (Fugloy Ridge) and (C) OBS 82 (oceanic crust). Positive offsets are SE of the OBS in question. Traveltimes are reduced at a velocity of  $7 \text{ km s}^{-1}$ . The position of each of these OBS is highlighted on the accompanying map.

and offset corrections were calculated for each shot into each OBS to correct for this off-line position and to replot the data as if the OBSs were all positioned on the line.

To test different gun-timing alignments, two passes were made along the OBS line; the first (from north to south) tuning the airguns on the main initial peak (peak tuning), the second (from south to north) tuning them on the first bubble pulse (bubble tuning). The reader is referred to Lunnon *et al.* (2003) for more details. For the purpose of this study, to find a wide-angle *P*-wave velocity model, the peak tuned vertical geophone component data set from the OBS was used.

The coincident streamer profile provides a clear image of the margin stratigraphy, with the Moho reflection visible extending across the oceanic crust and beneath the COT. Also at the COT can be seen clear SDR sequences interpreted as subaerially erupted basalt flows in the upper structure and lower crustal layering at depth (Spitzer *et al.* 2005). Over the Fugloy Ridge and on its flank, clear features of basalt flows such as foresets can be seen where the basalts flowed into deep water, as well as structure underneath the basalt. The joint interpretation of the towed streamer and OBS data sets affords unprecedented control on the structure of the margin, and thus insight into the conditions and processes at breakup time.

### 3 MODELLING METHOD

The profile was modelled taking a top-down approach, starting with the water column, and then the post-basalt sediments. The sediment

**Table 1.** Summary of modelling statistics. Oceanic refractions and Moho reflections refer to rays arriving into OBS 58-85, Continental refractions refer to turning rays arriving into OBS 1-14, Base-LVZ reflections refer to reflected rays from the base of the LVZ arriving into OBS 30-57, Basalt refractions refer to rays turning above the LVZ and arriving into OBS 15-57, Continental Moho reflections refer to rays arriving into OBS 1-57.

Phase	Traveltimes fitted	rms misfit (ms)
Oceanic refractions	24 086	95
Continental refractions	9266	148
Base-LVZ reflections	5287	97
Basalt refractions	13 397	93
Oceanic Moho reflections	9417	78
Continental Moho reflections	16 362	118

velocities were modelled from semblance data derived from the 12 km streamer profile. The remaining crustal structure was then estimated from traveltimes picked from OBS data, working down through the upper crustal structure, including the low-velocity zone (LVZ), previously recognized by Richardson *et al.* (1999), Fruehn *et al.* (2001), Flidner & White (2003), Spitzer *et al.* (2005) and Spitzer *et al.* (2008). Detailed statistics for the traveltime modelling are shown in Table 1.

#### 3.1 Water column and sediment modelling

To choose the best average water velocity for the profile, we used a sound-velocity profile and expendable Bathy-Thermograph (XBT)

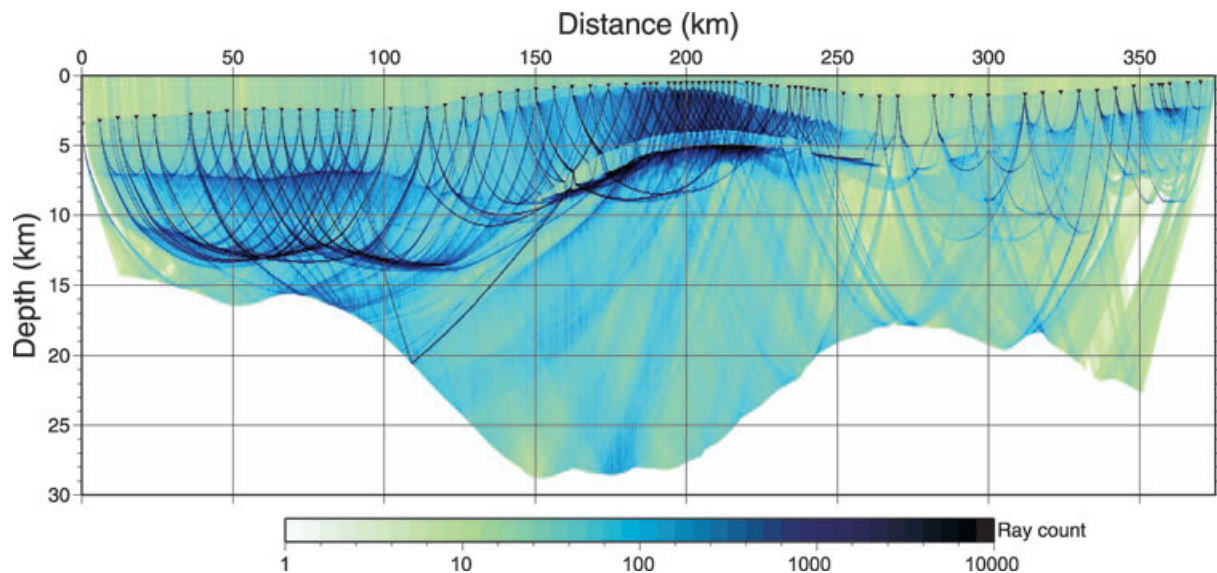


**Figure 3.** Ray coverage for the final model. Black triangles show the OBS positions. Ray count is the number of rays passing through each  $100 \text{ m} \times 100 \text{ m}$  cell.

data. A velocity of  $1.47 \text{ km s}^{-1}$  was found to be a suitable average over water depths to at least 700 m, which was the maximum depth of the sound-velocity profile. The velocity structure of the post-basalt sediments was modelled by smoothing velocity measurements produced from semblance picking of the 12 km streamer data by WesternGeco. This was done by plotting the picked 1-D velocity profiles versus depth below water bottom at each CMP position and fitting a sixth order spline through them for each of four regions of differing sediment velocity character along the line. The velocity functions for adjacent regions were merged by linearly mixing them over a distance of 20 km at the joins.

### 3.2 Modelling the upper crust

To model the upper crust, 45 749 traveltimes were made from the first arrival crustal refractions, as well as 5287 reflections from the base of the low-velocity zone. The ray density was very high in the basalt flows over the Fugloy Ridge and in the oceanic crust, meaning that the velocity structure in these regions could be well constrained (Fig. 3). The density of arrival time picks was lower in the continental crust of the Faroe-Shetland Basin due to the complex crustal structure, which made it difficult to identify phases.

An initial attempt to model the crust beneath the sediments was made using the First Arrival Seismic Tomography (FAST) inversion code of Zelt & Barton (1998). This code uses the finite difference least squares method, based on the work of Vidale (1990), to model first arrival traveltimes. The estimated picking error for the FAST inversion traveltimes was 130 ms. However, due to the presence of a low-velocity zone underneath the basalt on the Fugloy Ridge, FAST did not produce satisfactory results, and an inversion grid cell size of no smaller than  $5 \times 2 \text{ km}$  was necessary to prevent the inversion from becoming divergent. The reason was that on using a smaller inverse grid cell size there were more velocity and depth nodes than could be constrained by the traveltime step backs caused by the low-velocity zone (Fig. 4). The number of constrainable nodes is less in the presence of a low-velocity zone because, invoking Snell's Law, on entering a low-velocity zone the rays are bent towards the normal. Because no rays are able to turn upwards until at a higher velocity than that immediately above the low-velocity zone (i.e. rays

have passed through the low-velocity zone), the ray paths are all of similar incidence angles, which produces a strong velocity/depth trade-off within the low-velocity zone.

A forward-modelling approach using Rayinvr (Zelt & Smith 1992) was therefore adopted for the upper crustal structure, paying particular attention to modelling accurately the step back in the first arrival times, indicative of the low-velocity zone [see Figs 2b and 4 and Fliedner & White (2001a)]. Modelled traveltimes were fitted to within 100 ms of the picked times.

### 3.3 Basalt structure and extrusives at the COT

Some of the most prominent features on the streamer profile are the clearly defined SDRs at the COT (Spitzer *et al.* 2005; Parkin *et al.* 2007). Their well defined arcuate nature is consistent with subaerial extrusion. With the onset of seafloor spreading, crustal formation became submarine, and hence the reflector sequences become less well defined towards the north (Parkin *et al.* 2007). The basalt thickness decreases away from the COT, from a maximum thickness of around 7 km to the basalt feather edge in the Faroe-Shetland Basin (see Figs 5 and 6). The regional maps of White *et al.* (2003), which overlap with this profile south of the Fugloy Ridge, show good agreement with this profile. From Fig. 6, we see that towards the feather edge of the basalt (at 200–300 km along the profile), in the Faroe-Shetland Basin, the average velocity of the basalt section decreases, which is likely to be due to weathering and the thinning of the individual lava flows. As the flows become thinner, the percentage of high-velocity flow interiors decreases, so the overall velocity is decreased by the increasing influence of the lower velocity weathered flow tops and intra-flow sediments (Planke 1994).

#### 3.3.1 Low velocity zone

Reflected arrivals from the base of the LVZ were fitted using a forward-modelling approach, in conjunction with the sub-LVZ refractions. Due to the closeness in time of the turning rays and reflected rays, the traveltimes used for the inversions were picked carefully with an estimated uncertainty of 50 ms. After forward



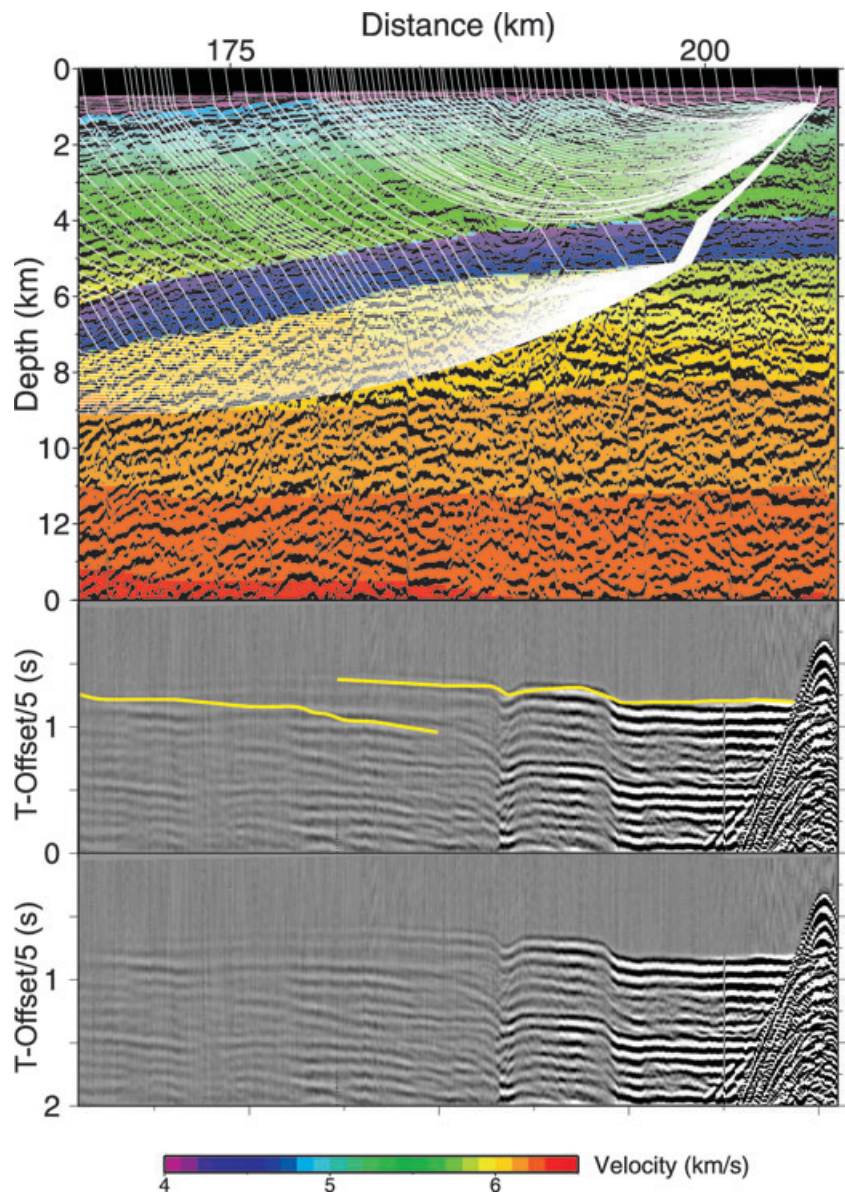


**Figure 4.** Raytracing through the velocity model with streamer profile overlaid (top panel), with associated ray-traced traveltimes overlaid on OBS gather (middle panel). OBS data and ray tracing are shown from OBS 44. As deep-propagating basalt turning rays encounter the top of a low-velocity zone they are bent towards the normal (Snell’s law). The rays do not turn within the LVZ, and so emerge at the base, into the basement below, where they turn upwards. As can be seen, the effect is to introduce a delay into the turning ray traveltimes, manifested as a step back on a seismic gather.

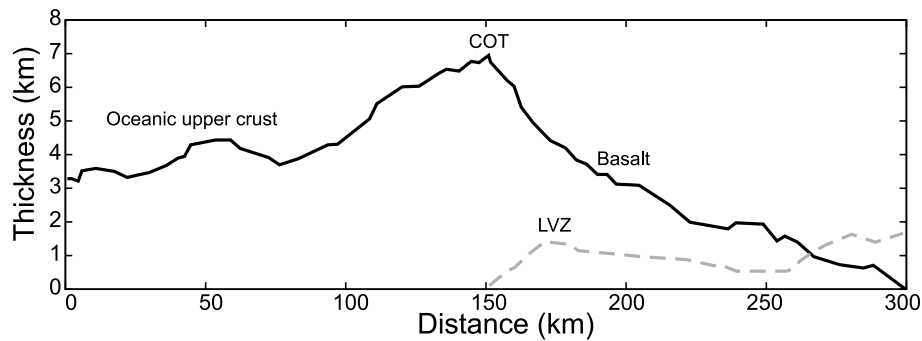


**Figure 5.** Extrusive basalt and sub-basalt Low Velocity Zone (LVZ) thicknesses versus distance along the line. On oceanic crust the basalt thickness is defined by the thickness of crust between the top of the basalt and the  $6.7 \text{ km s}^{-1}$  contour (i.e. the thickness of seismic Layer 2), and thins away from the COT as the oceanic crust becomes younger. Isovelocity lines are marked in Fig. 6.

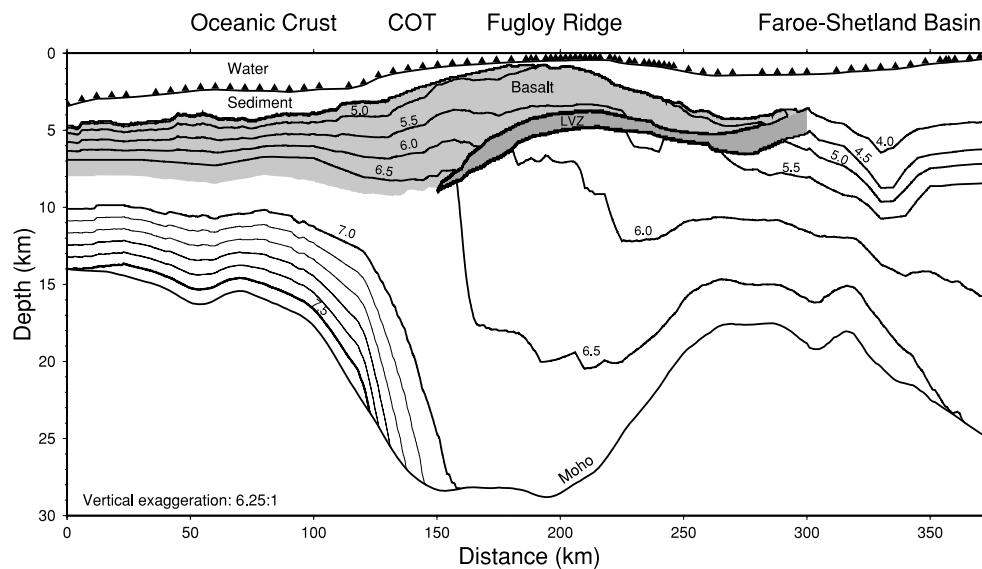


**Figure 6.** Modelled  $P$ -wave interval velocity model plotted against depth. Bold contours are shown every  $0.5 \text{ km s}^{-1}$  for velocities greater than  $4 \text{ km s}^{-1}$ . Light contours mark every  $0.1 \text{ km s}^{-1}$  between  $7.0$  and  $7.6 \text{ km s}^{-1}$ . Triangles show the OBS positions. Light and dark shading mark the basalt and LVZ, respectively, the thicknesses of which are plotted in Fig. 5.

modelling, single parameter inversions were carried out; the depth of the base of the low-velocity zone was inverted for using a range of fixed laterally constant LVZ velocities, then the velocity within the LVZ was inverted for using a range of fixed laterally constant thicknesses. It was clear early in this process that fitting rays for the second of these cases, with the LVZ thickness constant along the length of the LVZ, was highly problematic and geologically inappropriate, and so attention was focussed on the first case, inverting for the 2-D thickness along the profile for various fixed velocities within the LVZ. In each inversion case, a 'starting model' was generated for each fixed velocity by assigning an LVZ thickness at each point on the profile such that the traveltime step size was preserved in each case. Five inversion cycles were then carried out using two different smoothing lengths. The resulting rms misfit and number of modelled data points for each smoothing length were plotted as trade-off curves to determine a range of models which fitted the largest number of data points with the smallest rms misfit (Fig. 7). It is clear from these curves that there is a statistical preference towards a structure with a LVZ velocity of  $4.5 \text{ km s}^{-1}$ . The combined turning ray and base-LVZ reflection rms misfit of the best-fitting low-velocity zone structure (constant  $4.5 \text{ km s}^{-1}$ , variable thickness) was  $47 \text{ ms}$ , which is comparable to the average uncertainty of  $50 \text{ ms}$  in the traveltime picks.

The top of the low-velocity zone provides a clear marker as to the base of the overlying basalt, which means that an estimate of the volume of basalt extruded can be made by measuring the cross-sectional area of basalt assuming along-strike invariance. It is found to be  $380 \pm 40 \text{ km}^3 \text{ km}^{-1}$  on this profile. The uncertainty is calculated based on the estimated error of  $15 \text{ km}$  in measuring the lateral termination point of the basalt flows (which are very thin in the Faroe-Shetland Basin) and the error in the modelled basalt thickness of  $200 \text{ m}$  based on uncertainty in measuring the turning ray termination points on the OBS gathers (Flügel & White 2001a; Spitzer *et al.* 2005).

The low-velocity zone, first reported by Richardson *et al.* (1999), has now been mapped in detail for the first time all the way to the COT. The layer is approximately flat under the Fugloy Ridge, dips gently into the Faroe-Shetland Basin, but dips more strongly

towards the COT. This is consistent with the crustal thinning and subsidence caused by the continental breakup process. The low-velocity zone itself is thought, based on  $V_p/V_s$  studies, to comprise mainly sedimentary material (Eccles *et al.* 2007) but probably with some sill intrusion. In modelling a low-velocity zone, there is a strong trade-off between velocity and thickness (Flecha *et al.* 2004). However, as demonstrated in Fig. 7, statistical preference is found for a velocity of  $4.5 \text{ km s}^{-1}$ . Figs 4 and 5 show that the LVZ is typically  $1 \text{ km}$  thick, thinning towards the COT (consistent with crustal thinning and loading from the thick basalt lying above it at the time of continental breakup). Note that in two-way time (Fig. 8), the shape of the low-velocity zone deduced from the wide-angle data alone follows the MCS stratigraphy well. Spitzer *et al.* (2005) used a high resolution semblance technique to probe the basalt and LVZ structure on the southern flank of the Fugloy Ridge along the same profile. At  $215 \text{ km}$  they observed a sub-basalt LVZ thickness of  $1300 \text{ m}$ , thickening upslope (towards the COT). Our measurement at this point (Fig. 5) using the OBS data set is  $1000 \text{ m}$  thickness, also thickening upslope to a maximum of  $1400 \text{ m}$  at  $170 \text{ km}$ . From this point on, we model the LVZ thinning towards the COT at  $150 \text{ km}$ . Whereas there is likely to be better control on the thickness from the reflection data set used by Spitzer *et al.* (2005), it is clear that the thickness and trend presented here in Fig. 5 are broadly similar. Some discrepancy undoubtedly arises due to a lack of resolution using the OBS data set in being able to distinguish between the hyaloclastites and sediments, which are reported by Spitzer *et al.* (2005) as manifested by a two-stage velocity inversion. This blurring is a particular issue as the basalt thins to the feather edge, and is the likely cause of the thickening of the LVZ from  $260 \text{ km}$  downslope into the Faroe-Shetland Basin.

Because the low-velocity zone can be tracked to the COT, an obvious question is whether information about it can be gleaned from the conjugate margin near Kangerlussuaq, Greenland. Unfortunately no high-quality seismic profiles exist on the conjugate margin. However, stratigraphic work by Peate *et al.* (2003), Larsen *et al.* (1996) and Larsen *et al.* (1999), on the Kangerlussuaq Basin report the pre-breakup sedimentary structure based on surface exposures in the basin and they find laminated mudstones and

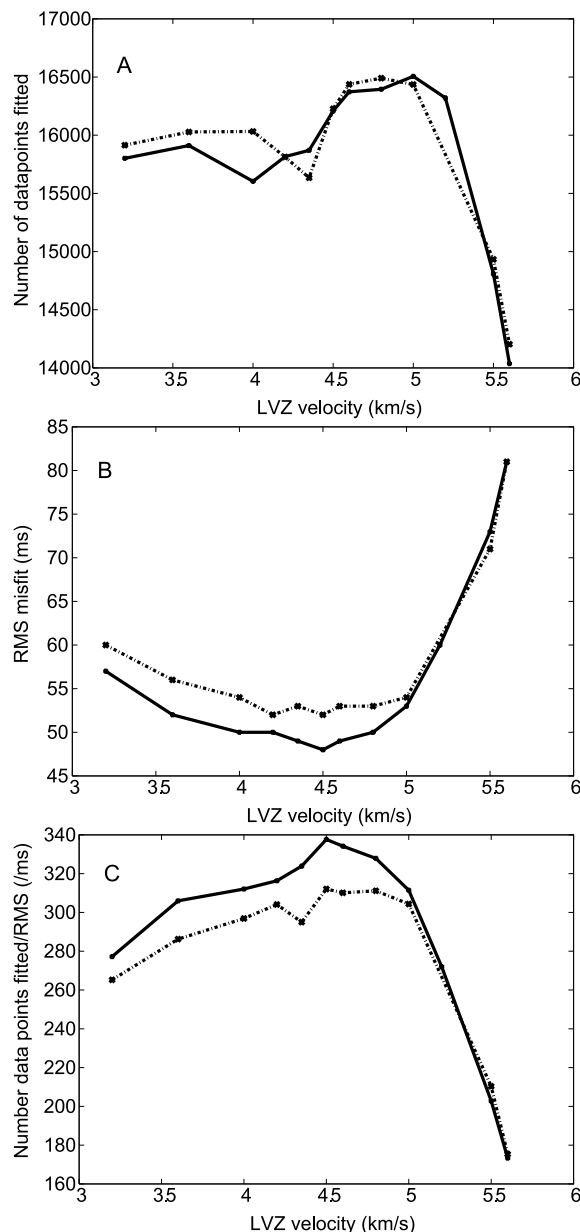


**Figure 7.** Modelling statistics for a variety of LVZ  $P$ -wave velocities. Note there is a clear bias, through a minimum in the misfit curve and a maximum in the fit-statistics, towards a velocity of  $4.5 \text{ km s}^{-1}$ . Results are shown using two different smoothing parameters in the inversion. Solid lines show results using a 3-point triangular averaging filter and broken lines show results using a five-point triangular averaging filter.

sandstones deposited from gravity flows. A time-converted form of the velocity model in Fig. 6 is shown in Fig. 8 and the velocity model is superimposed on the depth-converted seismic reflection profile in Fig. 9. The thinning of the LVZ in space is consistent with the thickening load of the basalt cover towards the COT. Immediately underneath the LVZ, there is good velocity control from the turning waves (standard error  $<0.1 \text{ km s}^{-1}$ ). Close to the COT, the immediate sub-LVZ velocity is  $6.0 \text{ km s}^{-1}$ , decreasing to  $5.5 \text{ km s}^{-1}$  under the Fugloy Ridge, consistent with the increased compaction and intrusion near the COT. These velocities are in agreement with the observations of  $5.50\text{--}5.65 \text{ km s}^{-1}$  for the top basement velocity under the thick basalt cover of Suduroy made by Richardson *et al.*

(1999). It can be seen from Figs 4 and 8 that there is a change in velocity gradient at about 2 km depth (0.75 s two-way time) below the LVZ stretching landward from 210 km (3 s two-way time, 8–9 km depth) and that this is associated with a change in reflectivity on the streamer profile. The onset of this feature is also associated with a change in reflective character of the LVZ, suggesting that a compositional change in the basement may be responsible for it. A strong reflector, stretching across the Fugloy Ridge at about 1.25 s below the low-velocity zone could represent the transition from Paleozoic and early Mesozoic rocks to Lewisian basement rock.

### 3.3.2 Synthetic modelling

To probe the structure in the vicinity of the low-velocity zone in more detail, and to assist in the identification of the various phases visible on the seismograms, 2-D elastic waveform modelling of the region under the Fugloy Ridge was carried out. Synthetic seismograms to 14 s time were produced for each OBS location down to 15 km depth, and out to offsets of 50 km on each side. The SEM2DPACK finite element elastic code (Ampuero 2008) was used to make the 2-D synthetic data. To verify the consistency of the results, a control test comparing traveltimes was performed for a 1-D model, using a Schlumberger proprietary code, PWTIM (a 1.5D elastic modeller based on the invariant embedding algorithm: Kennett 1974). This test showed good agreement between the traveltimes and amplitudes across the output seismograms. One of the drawbacks of using the SEM2DPACK code is that it will not allow an acoustic water layer. In this case, the  $S$ -wave velocity field was chosen to be simply  $V_p/\sqrt{3}$ , and so the modelled water  $S$ -wave could be identified as the slowest arrival on the gather ( $850 \text{ ms}^{-1}$ ). It also has limited capacity for modelling absorption, and so this was simulated for the arrivals of interest ( $P$ -wave or  $S$ -wave, travelling at around  $5 \text{ km s}^{-1}$ ) by applying an exponentially decaying gain with offset, computed using an effective  $Q$  value of 45 (Maresh *et al.* 2006; Shaw *et al.* 2008) to the synthetic gathers. This does not take into account variation of scattering with depth, and for energy propagating at large depths in comparison to the total offset, this is a poor approximation due to the actual distance travelled by the energy being significantly larger than the offset. However, for energy travelling at larger offsets as diving waves returned from the upper crust, with a comparatively large sub-horizontal path, this simple scaling provides a reasonable approximation to the effect of energy loss. A simple density field was used, with  $1000 \text{ kg m}^{-3}$  for water and post-basalt sediment layers and  $3000 \text{ kg m}^{-3}$  for the basalt and below.

Real and synthetic data sets for OBS 44 are shown in Fig. 10 both without (synthetic A) and with (synthetic B) attenuative gain applied. Note the importance of this; with only simple range scaling (synthetic A) it may be interpreted that there is focusing of seismic energy towards the base of the basalt, yet this is simply an effect of the offset-dependent gain, and is not apparent when attenuation is included (synthetic B). Agreement between the real and synthetic traveltimes can be seen from Fig. 4.

It can be seen from Fig. 10 that the base-LVZ reflection is clearly identifiable on the synthetic data sets, and is identifiable, but less clearly so on the real data set. The top-LVZ (base basalt) reflection is also visible on the synthetic though it is weaker, and is only faintly visible on the real data. This suggests that, particularly in the case of the top-LVZ reflection, the impedance contrast may be lower than that modelled using traveltimes.

On the southern (right hand) side of the gather, the sub-basalt turning wave is also relatively strong on the synthetic compared to



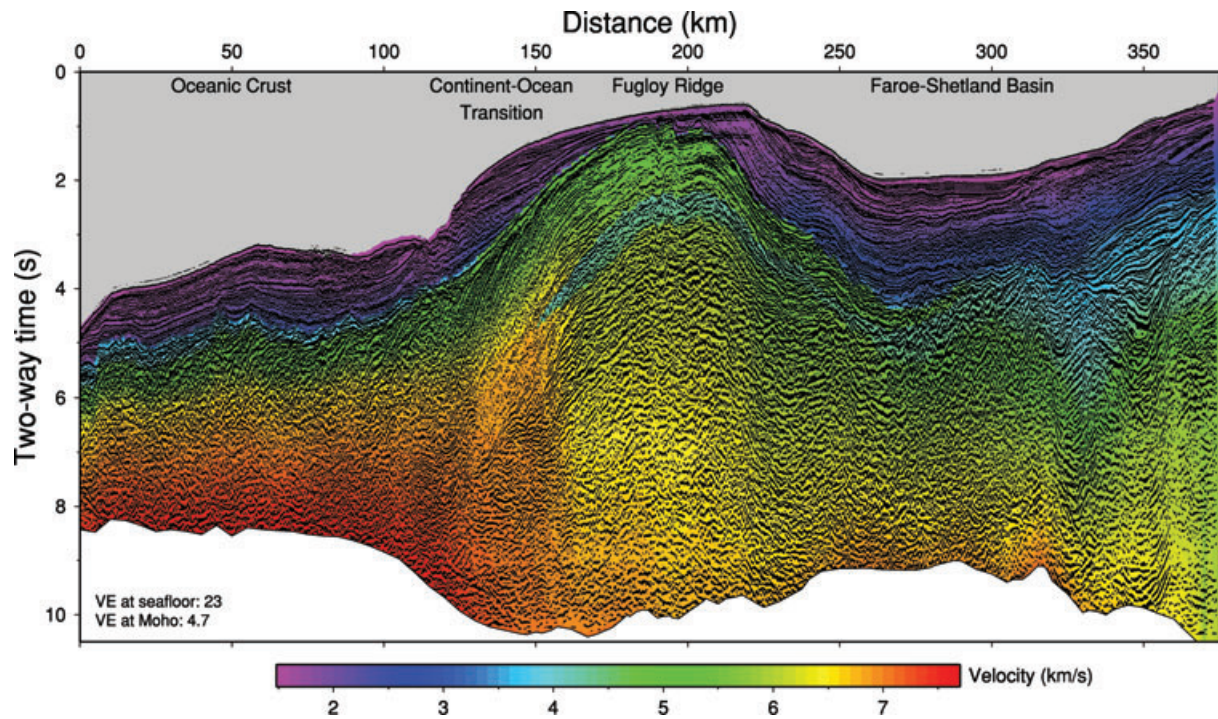


**Figure 8.** Velocity model from Fig. 6 plotted against two-way time and overlain on the coincident seismic reflection profile. Reflection data courtesy of WesternGeco. Processing includes deconvolution, 40 Hz low-pass and F-K filtering, geometric spreading correction, Kirchhoff surface multiple removal, Radon filter and pre-stack time migration. Details are in Spitzer *et al.* (2005). In addition a time-gain is applied to the deep region.

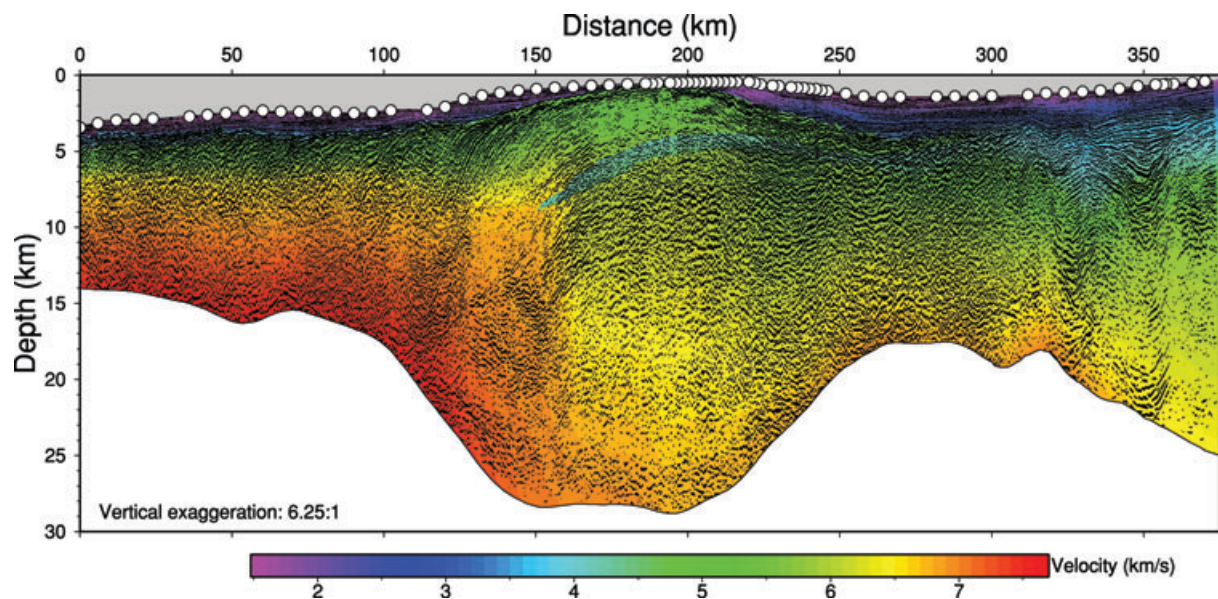


**Figure 9.** Final velocity model from Fig. 6 overlain by the depth-converted Q streamer profile. The base of the model is the Moho reflector as modelled using the OBS data set. Circles show OBS positions.

the real data. On both sides the basalt turning wave remains strong in amplitude, and the termination points on the real and synthetic data match well, which suggests that the attenuation is produced by a lateral change in character of the hyaloclastic/sedimentary low-velocity zone or basement.

### 3.4 Faroe-Shetland Basin

This profile does not just cross a continental margin, but also a region where considerable extension occurred at an earlier time, the

Faroe-Shetland Basin. The task of modelling this region was made difficult by the complicated continental crustal structure (such as due to sill intrusion, for example), by high attenuation and by high velocity-gradients causing turning rays to be seen only out to small (20 km or so) offsets (Fig. 2). Constraint is thus poorer in this region than along the rest of the profile (Fig. 3). However, some crustal velocity control was obtained, primarily by modelling the Moho reflections which were visible on some OBS gathers. The Moho depth also compared well to that found by gravity modelling of the area (personal communication with A. Chappell, 2008). By



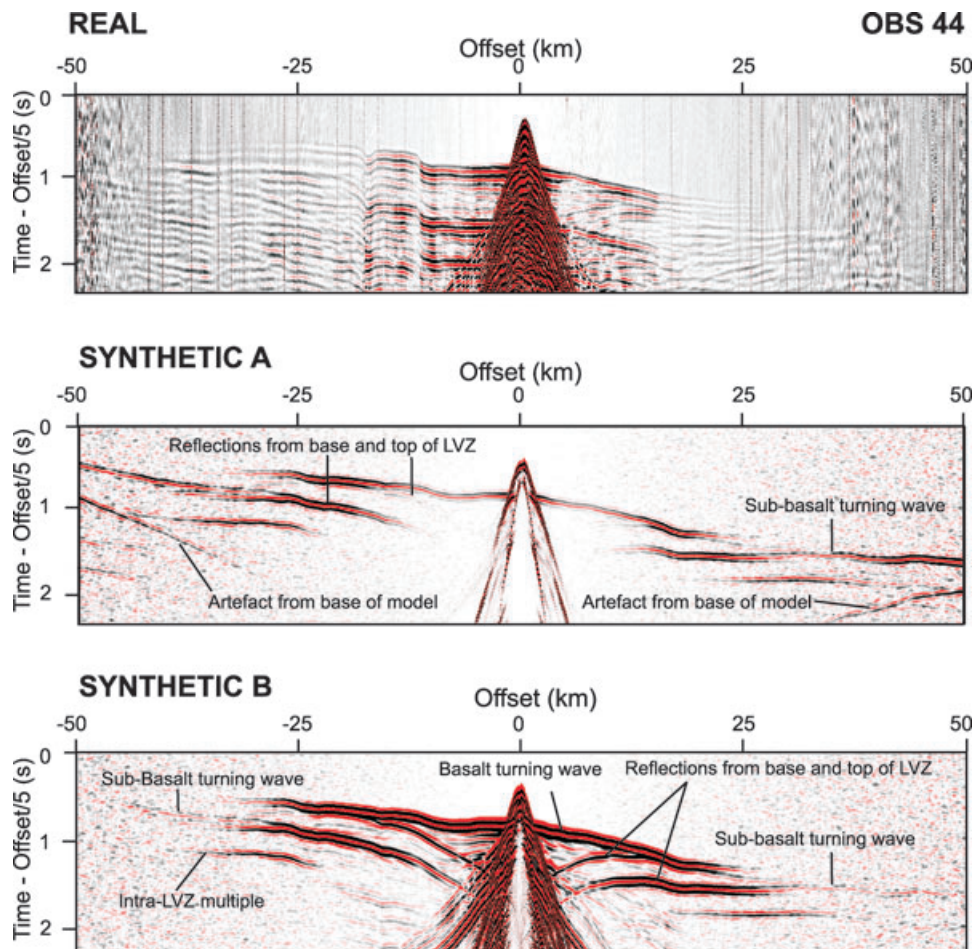


**Figure 10.** Real and synthetic OBS gathers for OBS 44 (vertical component). To generate the synthetic data, a time sampling of 0.4 ms was used to keep the simulation stable. This was then down-sampled to 4 ms (the sampling used for the real data). A Ricker wavelet was used with peak and maximum frequencies of 8 and 15 Hz, respectively. The shooting geometry used to produce the synthetic seismograms, as for the traveltimes modelling, was reciprocal to that used for the real survey. The synthetic receiver spacing (corresponding to shots in the real domain) was 100 m. The raw synthetic gathers were produced without attenuation or noise (Section 3.3.2). To compare the real and synthetic data sets the following processing was applied. Both real and synthetic data were reduced at  $5 \text{ km s}^{-1}$ . To produce the REAL data set, a gain was then applied which is linearly proportional to offset. To produce SYNTHETIC A, after reducing at  $5 \text{ km s}^{-1}$ , Gaussian noise was added (signal-to-noise ratio of 200), followed by applying the same offset-dependent gain which was applied to the REAL data set. To produce SYNTHETIC B, the data were reduced at  $5 \text{ km s}^{-1}$ , before applying an exponential gain of the form  $\exp\left(\frac{-\pi f x}{v Q}\right)$  where  $f$  is a representative frequency (chosen to be 10 Hz),  $v$  is a representative seismic velocity, chosen to be  $5 \text{ km s}^{-1}$ ,  $Q$  is the effective quality factor, chosen as 45 (Mares *et al.* 2006; Shaw *et al.* 2008), and  $x$  is the offset. The same Gaussian noise and linear gain in offset applied to SYNTHETIC A were then also applied to SYNTHETIC B. The data sets were then panel-gained up or down to be visually comparable. No time-dependent gain was applied to any of the data sets.

comparing the thinnest point of the basin (9 km basement crustal thickness at 330 km distance) to the unstretched crustal thickness underneath Scotland of 30 km (there are no completely unstretched areas on our profile) (Fowler 2004), one obtains a  $\beta$  value of  $3.3 \pm 0.1$ . Christie (1982) obtained a crustal thickness of 32 km under the East Shetlands Platform, which yields a  $\beta$  value of  $3.52 \pm 0.1$ . These stretching factor estimates suggest that the basin was close to rupture. Uncertainty in this value is based on an estimated error of 1 km in measuring the crustal thickness at the thinnest point in the basin caused by possible mis-identification of the Moho and the top of the crust at the time of stretching due to high reflectivity in the region. The velocity model shows that velocities reach  $7.0 \pm 0.3 \text{ km s}^{-1}$  at the base of the crust in the Faroe-Shetland Basin. Accompanying these velocities, the MCS profile clearly shows some reflectivity in association with this high velocity crust (Figs 8 and 9). Crustal reflectivity has also been reported in the Faroe-Shetland Basin by Raum *et al.* (2005), among others, though they did not have sufficient resolution to detect such layering in the deep crust. This

suggests that some intruded sills are present, probably associated with the crustal stretching.

Moho reflections under the Faroe-Shetland Basin are clearly visible on a number of OBS, although on others the sills and other complexities in the continental crustal structure made Moho events hard to identify. However, it was possible using these reflections to map the Moho under the Faroe-Shetland Basin and the Fugloy Ridge. On the streamer profile, the Moho reflection is not obvious in this region, although a tentative Moho reflection was identified based on the Moho observed from the wide-angle data set.

### 3.5 Deep structure: intrusives at the COT and the Moho

Control on the deeper velocity structure was afforded from a combination of deep turning rays (mainly in the region of oceanic crust and the COT), as well as from Moho reflections, visible on the wide-angle data set along the line.

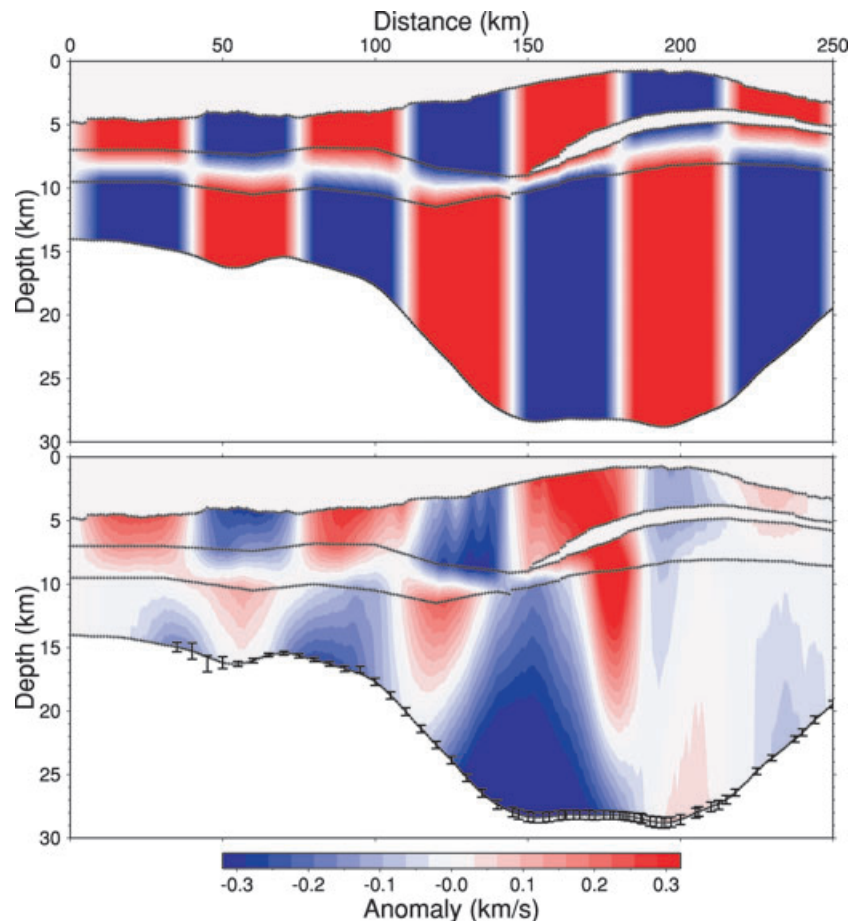


**Figure 11.** Checkerboard velocity anomalies. The velocity model from Fig. 6 was perturbed using the anomaly shown in the upper plot (a). Synthetic traveltimes were then generated. Several inversion cycles were then performed using Rayinvr (Zelt & Smith 1992) with the unperturbed velocity distribution as a starting model and the synthetic traveltimes as the target. The recovered anomaly is shown in the lower plot (b). Crosses mark 1 km model nodes. Representative error bars show the uncertainty in recovered Moho depth.

### 3.5.1 Deep turning rays

Away from the region of basalt flows over sediment, such as the oceanic crust and through the COT, turning rays propagate at depth, and these provided good constraint on the seismic velocities in these regions. Modelling the oceanic crust, basalt, and sub-LVZ refractions was thus quite straightforward and good velocity control was obtained particularly in the oceanic crust (Figs 3 and 11). The picking error assigned for the forward modelling of these turning ray traveltimes was 100 ms, smaller than that used for the FAST inversion input traveltimes because in the course of forward modelling, updates of the picks were carried out from time to time.

### 3.5.2 Moho reflections

25 779 Moho reflection picks were made along the line, with a greater density at the oceanic end and the COT, where the Moho reflections were very clear (Figs 2 and 3). These traveltimes were forward modelled using Rayinvr. Again, modelling the oceanic crust and COT regions was much more straightforward than was the Faroe-Shetland Basin due to a much less complicated wide-angle arrival structure. The large number of crossing rays in the COT (Fig. 3) meant that good velocity constraint was obtained in this region. Where there were deep turning rays (in the oceanic crust and COT), joint forward modelling was performed of the two phases.

The Moho depth and velocity structure in the deep part of the crust were subsequently smoothed by taking the mean velocity field and the Moho from the results of inverting for the Moho reflections and deep turning rays using 20 different sets of perturbed (from the forward model) starting velocity fields, Moho and traveltime picks. The final forward model  $\chi^2_{\text{refractions}}$  was 1.05 and  $\chi^2_{\text{reflections}}$  was 1.10, and a comparison of the output traveltimes with those from the early FAST modelling is shown in Fig. 12, showing the improvement in the final model. The error bars on the Moho depth in Fig. 11b show the spread of Moho depths calculated from this suite of inversions with randomized starting models. As with the turning rays, the estimated picking error for the Moho reflections was 100 ms.

### 3.5.3 Checkerboard test

A checkerboard test was used to assess the trade-off between velocities at the nodes of the model. This was carried out by taking the final velocity model (Fig. 6), applying a periodic perturbation, as shown in Fig. 11(a), and generating synthetic traveltimes. The unperturbed model was then used as a starting model to invert the perturbed traveltimes and the result compared to the true perturbed model (Fig. 11b).

To give a comparable result across the profile, the model nodes were evenly sampled with 1 km spacing, as shown by the crosses

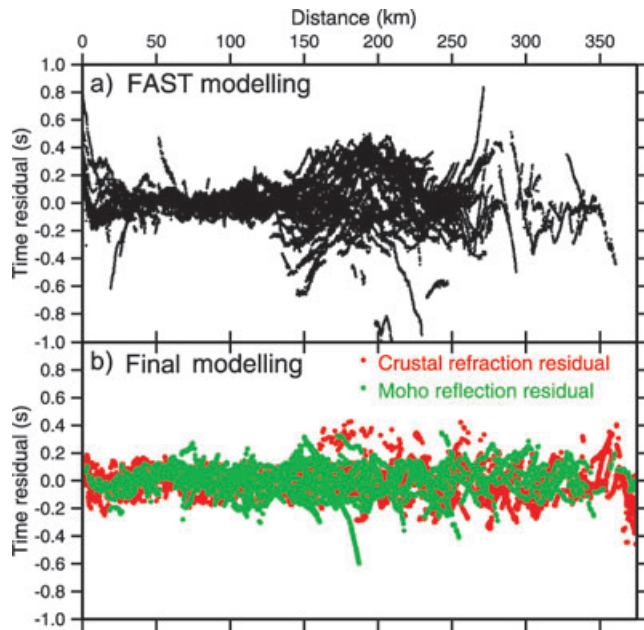


**Figure 12.** Traveltime residuals for crustal refractions and Moho reflections, from (a) FAST modelling of first arrivals only, (b) semblance velocities for sediments combined with Rayinvr forward modelling.

on Fig. 11. The perturbations were generated as uniform bands of  $\pm 0.3 \text{ km s}^{-1}$  of 15 km width, with alternating polarity, mixed over a distance of 10 km, and therefore, with a total horizontal wavelength of 50 km. Vertically, opposite polarity anomalies were generated at the top and bottom of the model, and linearly mixed between two boundaries in the Rayinvr model, corresponding to the base basalt and a region several kilometres under the LVZ. The ocean layer, post-basalt sediments and sub-basalt low-velocity zone were left unperturbed (Fig. 11).

Synthetic traveltimes for each OBS were generated by raytracing through this model. An inversion scheme was then devised using the Rayinvr inversion routine (Zelt & Smith 1992). The unperturbed model was used as the starting model with inversions to adjust the model to fit the synthetic traveltimes. The inversion scheme fitted turning rays progressively down through each layer of the model, and finished by fitting the Moho reflections. Two inversion cycles were carried out for each layer, with a 5 km smoothing filter applied after each step. At each stage the layers above the layer currently being inverted for were held fixed.

It can be seen that there is a degree of smearing at depth in the COT, but that the deep crust is reasonably well resolved from the continental crust of the Fugloy Ridge to the oceanic crust (i.e. from 0 to 200 km distance along the profile).

### 3.5.4 Intrusion at the continent–ocean transition

The availability of a high quality deep seismic reflection profile coincident with the wide-angle line allows us to constrain the total volume of igneous rock intruded and extruded on the continental margin during breakup. On the streamer profile (Fig. 8), on the landward side of the Fugloy Ridge, basalt foresets are clearly visible, representing the building of a paleo-shoreline. Spitzer *et al.* (2005) have probed the fine scale basalt velocity structure, as well as characterising the low-velocity zone in this region using semblance techniques. Underneath the SDRs at the COT, considerable layering can be seen at depth in the mid-crustal region. Figs 8 and 9 show that

this deep layered material has a seismic velocity of  $> 6.8 \text{ km s}^{-1}$ . The velocity uncertainty in this region is  $< 0.1 \text{ km s}^{-1}$ , although as can be seen in Fig. 11, the spatial resolution of the velocity structure decreases at depth. The fact that the velocity is higher than the maximum found for continental crust implies that some igneous material with its characteristically higher velocity is present in this region, and the fact that layering is observed on the streamer profile in the same area strongly suggests that the intrusion is in the form of sill-like structures.

The other striking feature of this profile is that the COT is very narrow, with the transition from continental to oceanic crust taking place over a distance of only 50 km. This is also seen on the Hatton Bank iSIMM profile (White *et al.* 2008; White & Smith 2009), which was modelled completely independently. On the streamer profile, the deep structure under the Fugloy Ridge appears comparatively featureless compared to that of the COT. One likely cause of this is masking by the heterogeneous basalt structure, but because of the well constrained sharp velocity transition at the COT, it is reasonable to deduce that the degree of intrusion is much less than near to the COT. One can, therefore, infer that the lateral intrusion of melt was quite limited. The inferred sills cross-cut the dipping fabric of the country rock.

The velocity structure of the lower crust at the COT can be used to constrain the percentage of intruded igneous rock, provided that the velocity structure of pristine (unintruded) continental crust is known, as is the velocity of the material which is intruded. If the crustal section under the Fugloy Ridge at 200 km distance along the profile is assumed to be the end-member that represents continental crust, whereas the first-formed oceanic crust at 120 km along the profile represents the fully igneous section, then by a simple mixing law the percentage of each component can be calculated at every point across the COT region between them. This can be seen graphically in the velocity–depth profiles shown in Fig. 13. At the centre of the COT (150 km along the profile), lower-crustal velocities are intermediate between those of the continental and oceanic crust.

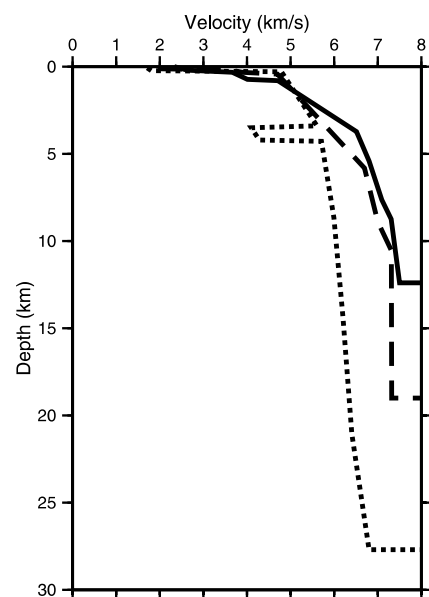


**Figure 13.** Velocity profiles through oceanic (solid), transitional (long dashes) and continental crust (short dashes). The distances along the line (Fig. 6) at which these profiles are taken are 50 km, 120 km and 200 km, respectively. Profiles are plotted against depth below base of sediments.



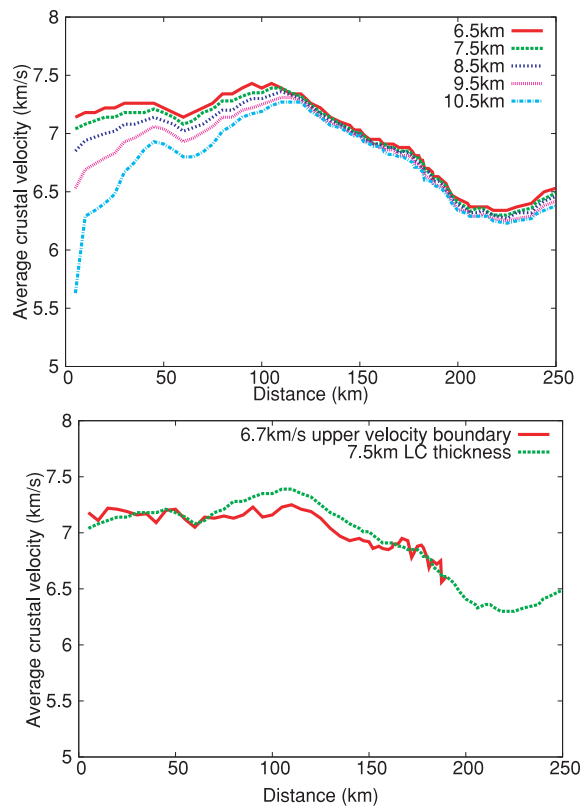


**Figure 14.** Average crustal velocity calculated over regions of varying heights above the Moho (top), and comparison using a 7.5 km constant thickness as opposed to the  $6.7 \text{ km s}^{-1}$  velocity contour (bottom).

In Fig. 14 we show two different ways of calculating the average velocity of the lower-crust which give results that are little different whichever is adopted. One method is to calculate the average velocity of a fixed thickness above the Moho, as we show in the top panel of Fig. 14. For a lower-crustal layer thickness varying from 6.5 to 9.5 km, the results are indistinguishable across the continental and COT sections. The curves diverge across the oceanic section, primarily because as the oceanic crust thins towards the younger crust (approaching 0 km distance), the fixed thickness encroaches further into the extrusive upper crust until, at 0 km distance the thickness of 9.5 km includes the entire oceanic crust whereas the thickness of 10.5 km includes sediments too (Fig. 9). The average velocity is, accordingly, greatly reduced approaching 0 km distance. However, the important observation for our purposes is that the average velocity across the COT varies little whether we measure it across the lower 6.5 km or the lower 10.5 km of the crust (Fig. 9).

An alternative method of constraining the lower-crustal velocity which is better in the oceanic crust but not appropriate for the COT or continental crust is to measure the average velocity beneath the distinctive change in slope on the velocity-depth curve that marks the top of oceanic seismic layer 3. This is at a velocity of  $6.7 \text{ km s}^{-1}$ , as on the lower panel of Fig. 14, on which is shown a comparison between the average lower-crustal velocity beneath the  $6.7 \text{ km s}^{-1}$  contour and a uniform thickness of 7.5 km.

On the oceanic section of the profile, which covers the first 10 Ma of seafloor spreading, there is a systematic decrease in igneous crustal thickness which is accompanied by an overall decrease in average lower-crustal velocity. Both can be interpreted as due to a decrease in mantle temperature of about  $75^\circ\text{C}$  during the first 10 Ma

after continental breakup (Parkin *et al.* 2007; White *et al.* 2008). The upper oceanic crustal thickness (Fig. 5) shows a complementary systematic decrease as the crust becomes younger away from the COT.

Across the COT, the average lower-crustal velocity increases from  $6.8 \text{ km s}^{-1}$  to  $7.4 \text{ km s}^{-1}$  (Fig. 14a) as the percentage of intruded igneous rock increases from zero (on the continental side) to 100 percent (on the oceanic side). To estimate the volume of intruded rock, the fraction of intruded rock at each point of the model through the transition region was estimated using the velocity as a constraint. The first step was to transform the velocities to what they would be at a fixed pressure of 230 MPa and a temperature of  $150^\circ\text{C}$  to remove the main effects of changes in velocity with depth due to pressure and temperature increases. This was done using the method of Korenaga *et al.* (2002).

To calculate the fraction of intrusion at a given point, reference velocities must be calculated for the cases of 100 and 0 percent intrusion. The reference igneous section representing 100 percent plutonic rock was taken from the oceanic profile at 120 km distance along the profile, using the lower-crustal velocities beneath the  $6.7 \text{ km s}^{-1}$  contour which marks the top of oceanic layer 3. Because the Moho depth varies between 22 and 29 km across the COT, the oceanic velocity profile was stretched from a depth of 9.7 km (which is the average depth of the  $6.7 \text{ km s}^{-1}$  contour under the SDRs) to the base of the crust at each distance across the COT where the proportion of intruded rock was calculated. In a similar manner, the velocity profile representing zero intrusion (pure continental crust) was taken as the velocity-depth profile at 200 km distance along the profile, modified at depths greater than 22.8 km by extrapolating downward the velocity gradient from the crust above that depth to remove an increase in the velocity-gradient near the base of the crust which may be due to intrusion. The pure continental reference profile was then calculated at each distance through the COT by stretching this profile from 9.7 km down to the Moho depth.

Using these reference profiles, the intrusion fraction  $x$  was calculated throughout the transition region (Fig. 15) using the following isostress relation derived from calculating the average velocity  $v_{\text{avg}}$  for two linearly mixed phases  $v_1$  and  $v_2$  where  $x$  is the fraction of material with velocity  $v_2$  present:

$$x = \frac{v_2(v_{\text{avg}} - v_1)}{v_{\text{avg}}(v_2 - v_1)}.$$

To calculate the total amount of intrusion this fraction is integrated over the transition region. We also varied the velocities of both the reference profiles by  $\pm 0.1 \text{ km s}^{-1}$ , which is the estimated uncertainty, to allow us to calculate the limits of the volumetric intrusion. This gives a total volume of intrusion across the COT of  $560\text{--}780 \text{ km}^3$  for every kilometre of strike along the profile. By adding this to the volume of extruded material calculated in Section 3.3.1 ( $380 \pm 40 \text{ km}^3 \text{ km}^{-1}$ ), the combined volume of igneous material intruded and extruded during continental breakup is, therefore,  $900\text{--}1200 \text{ km}^3 \text{ km}^{-1}$ . This is likely to be a minimum estimate because there are indications of high velocities possibly representing igneous intrusions at the base of the crust beneath both the Fugloy Ridge and the Faroe-Shetland Basin (Fig. 9). There is a region of more than 90 percent intrusion immediately under the extrusive layer on the COT (Fig. 15). This probably represents the high-level magma chambers from which the basalts were extruded. At greater depths below 12 km the percentage of intrusion is lower and the crust is likely to be a mixture of intruded igneous rock and stretched continental crust.

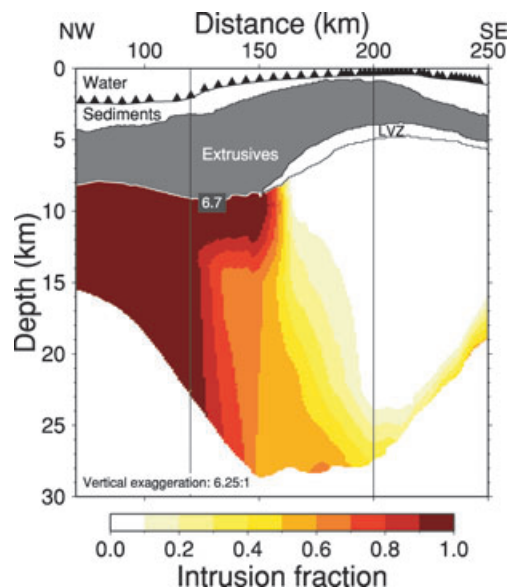


**Figure 15.** Distribution of intruded material through the COT. By integration for every kilometre along strike the total volume of intrusion at the COT (landward from 120 km) is  $560\text{--}780\text{ km}^3\text{ km}^{-1}$  and the volume of extruded rock is  $380 \pm 40\text{ km}^3\text{ km}^{-1}$ , giving a total igneous volume of  $900\text{--}1200\text{ km}^3\text{ km}^{-1}$ . Vertical lines at 120 km and 200 km show the position of the reference profiles chosen to represent 100 percent and 0 percent intrusion, respectively.

From Fig. 9 it can be seen that the most prominent lower-crustal reflectivity at the COT is actually in the mid-crust, rather than near to the Moho. The fact that the Moho is clearly visible at the base of the COT means that the lack of reflectivity in the bottom part of the crust here is not a result of the seismic energy being absorbed, but is due to an absence of strong impedance contrasts. It should also be noted that, aside from the Moho reflection, there is no strong reflectivity in the lower part of the oceanic crust either. This is consistent with the assertion that the greatest level of reflectivity is seen where there are a lot of interfaces with high impedance contrasts such as are created in the mid-crust where igneous sills with high  $P$ -wave velocities intrude continental crust with much lower velocities (McBride *et al.* 2004).

### 3.5.5 The Moho

On the wide-angle data the Moho reflection was observed on a sufficient number of OBS to constrain its depth estimate along the entire profile. It was much more distinct, and therefore easier to identify, however, on OBS at the oceanic end and through the region of the COT. On the streamer profile, the Moho was also distinct at the oceanic end and through the COT, though not obvious along the rest of the profile. However, hints of Moho reflections are seen under the Faroe-Shetland Basin, but these are difficult to identify due to the complex structure in this region. There are two possible reasons why the Moho becomes much less distinct under the Fugloy Ridge and the Faroe-Shetland Basin, but is much more visible at the oceanic end and at the COT. First, it could be that complex continental structure causes much seismic energy, particularly sub-critical energy, to be lost or scattered. This is particularly the case over the Fugloy Ridge, where there is significant basalt cover, and also where comparison of the real and synthetic data sets shows that there is increased attenuation from the LVZ downwards (Section 3.3). Sec-

ond, it is possible that the Moho interface significantly changes in character between the oceanic crust and the continental crust, from a sharp interface at the oceanic end to a gradational change under the continental region.

The BIRPS profiles of the 1990s (Klemperer *et al.* 1992) show a range of continental Moho reflectivity types in the region of the British Isles. Often the Moho is defined not as a single reflector, but as the base of the region of lower crustal reflectivity. If the Moho were more gradational in character beneath the continental crust on this profile, then this would be consistent with other areas of Britain, and with the fact that the oceanic Moho is considerably younger than is the continental Moho.

## 4 CONCLUSIONS

We have shown that complementary use of a deep sub-critical MCS reflection data set with a well constrained wide angle velocity model provides a powerful interpretative tool for investigating the deep structure of continental margins.

Although it is difficult to determine the velocity structure inside a low-velocity zone, some statistical constraint has been possible in this case. This has constrained the velocity to be  $4.5 \pm 0.6\text{ km s}^{-1}$ . The appearance of the traveltime step on the OBS records from the vicinity of the Fugloy Ridge shows that this low-velocity zone extends up to the COT. The modelling of reflections from the base of the LVZ, combined with synthetic waveform modelling, suggests that the base of the LVZ has been successfully mapped.

Lower-crustal layering at the COT, under clearly imaged SDR sequences, has been unambiguously imaged and associated with  $P$ -wave velocities of  $6.7\text{--}7.4\text{ km s}^{-1}$ . The reflectivity at the COT has been observed as greatest in the mid-crust, consistent with the maximum reflectivity being where there is a substantial amount of both continental and igneous crust present. The COT in this region near to the Faroe Islands is only around 50 km wide, similar to that at Hatton Bank (White *et al.* 2008). Using the velocity profile in conjunction with the streamer data has allowed an estimate of the total amount of intruded and extruded rock to be made.

The volume of intrusion at the COT has been estimated from the velocity model as  $560\text{--}780\text{ km}^3$  per kilometre along strike. Adding this to the volume of extruded rock of  $380 \pm 40\text{ km}^3\text{ km}^{-1}$ , estimated from the thickness of basalts imaged on the reflection profile, gives a total volume of igneous rock of  $900\text{--}1200\text{ km}^3\text{ km}^{-1}$ .

The Moho has been imaged clearly at the base of the oceanic and transitional regions on both the towed streamer and OBS data sets, and less prominently on the OBS data set under the Fugloy Ridge and into the Faroe-Shetland Basin. The change in reflective Moho strength along the line is probably due to the difference between the sharp, newly formed crust–mantle transition at the oceanic end and the old, probably multiply reworked and intruded base of the crust beneath the Archean rock at the continental end of the profile.

## ACKNOWLEDGMENTS

iSIMM is supported by Liverpool and Cambridge Universities, Schlumberger Cambridge Research, Badley Geoscience Ltd, WesternGeco, Amerada Hess, Anadarko, BP, ConocoPhillips, ENI UK, Statoil, Shell, the Natural Environment Research Council and the Department of Trade and Industry. We are grateful to the officers and crew of the RRS Discovery and to the technicians and scientists who assisted at sea. The 85 four-component OBS were provided by GeoPro GmbH and the towed streamer acquisition by WesternGeco.

The authors would like to thank Tony Doré, as well as an anonymous reviewer for their enthusiastic and helpful comments. Department of Earth Sciences contribution number ESC900.

## REFERENCES

- Abrahamsen, N., Schoenharting, G. & Heinesen, M., 1984. Paleomagnetism of the Vestmanna core and evolution of the Faroe Islands, in *The Deep Drilling Project 1980–1981 in the Faeroe Islands*, pp. 93–108, eds Berthelsen, O., Noe-Nygaard, A. & Rasmussen, J., AiO Print, Odense, Denmark.
- Ampuero, J.-P., 2008. SEM2DPACK, A Spectral Element Method tool for 2D wave propagation and earthquake source dynamics, Users Guide, Version 2.3.0, [http://web.gps.caltech.edu/ampuero/software/users\\_guide\\_sem2dpack.pdf](http://web.gps.caltech.edu/ampuero/software/users_guide_sem2dpack.pdf).
- Barton, A.J. & White, R.S., 1997. Crustal structure of Edoras Bank continental margin and mantle thermal anomalies beneath the North Atlantic, *J. geophys. Res.*, **102**, 3109–3129.
- Breivik, A.J., Mjelde, R., Faleide, J.I. & Murai, Y., 2006. Rates of continental breakup magmatism and seafloor spreading in the Norway Basin–Iceland plume interaction, *J. geophys. Res.*, **111**, doi:10.1029/2005JB004004.
- Christie, P.A.F., 1982. Interpretation of refraction experiments in the North Sea, *Phil. Trans. R. Soc. Lond. A*, **305**, 101–112.
- Christie, P.A.F., Gollifer, I. & Cowper, D., 2006. Borehole seismic studies of a volcanic succession Lopra-1/1A borehole in the Faroe Islands, NE Atlantic *Geol. Denmark Surv.*, **9**, 23–40.
- Coffin, M. & Eldholm, O., 1994. Large igneous provinces: crustal structure, dimensions, and external consequences, *Rev. Geophys.*, **32**(1), 1–36.
- Cox, K.G., 1980. A model for flood basalt vulcanism, *J. Petrol.*, **21**, 629–650.
- Eccles, J.D., White, R.S., Roberts, A.W., Christie, P.A.F. & iSIMM team, 2007. Wide-angle converted shear wave analysis of a North Atlantic volcanic rifted continental margin: constraint on sub-basalt lithology, *First Break*, **25**, 63–70.
- Eldholm, O. & Grue, K., 1994. North Atlantic volcanic margins: dimensions and production rates, *J. geophys. Res.*, **99**, 2955–2968.
- Flecha, I., Marti, D., Carbonell, R., Escuder-Viruet, J. & Pérez-Estaún, A., 2004. Imaging low-velocity anomalies with the aid of seismic tomography, *Tectonophysics*, **388**, 225–238.
- Flidner, M.M. & White, R.S., 2001a. Sub-basalt imaging in the Faeroe–Shetland basin with large-offset data, *First Break*, **19**, 247–252.
- Flidner, M.M. & White, R.S., 2001b. Seismic structure of basalt flows from surface seismic data, borehole measurements, and synthetic seismogram modelling, *Geophysics*, **66**, 1925–1936.
- Flidner, M.M. & White, R.S., 2003. Depth imaging basalt flows in the Faeroe–Shetland Basin, *Geophys. J. Int.*, **152**, 353–371.
- Fowler, C.M.R., 2004. *The Solid Earth*, 2nd edn, Cambridge University Press, Cambridge, UK.
- Fowler, S.R., White, R.S., Spence, G.D. & Westbrook, G.K., 1989. The Hatton Bank continental margin, II. Deep structure from two-ship expanding spread seismic profiles, *Geophys. J.*, **96**, 295–309.
- Fruehn, J., Flidner, M.M. & White, R.S., 2001. Integrated wide-angle and near-vertical subbasalt study using large-aperture seismic data from the Faeroe–Shetland region, *Geophysics*, **66**, 1340–1348.
- Hinz, K., 1981. A hypothesis on terrestrial catastrophes–wedges of very thick oceanward dipping layers between passive continental margins; their origin and paleoenvironmental significance, *Geologisches Jahrbuch Reihe, E* **22**, 3–28.
- Holbrook, W.S. *et al.*, 2001. Mantle thermal structure and active upwelling during continental breakup in the North Atlantic, *Earth planet. Sci. Lett.*, **190**, 251–266.
- Hopper, J.R., Dahl-Jensen, T., Holbrook, W.S., Larsen, H.C., Lizarralde, D., Korenaga, J., Kent, G.M. & Kelemen, P.B., 2003. Structure of the SE Greenland margin from seismic reflection and refraction data: implications for nascent spreading center subsidence and asymmetric crustal accretion during North Atlantic opening, *J. geophys. Res.*, **108**, 2269–2291.
- Kennett, B.L.N., 1974. Reflections rays and reverberations, *Bull. seism. Soc. Am.*, **64**, 1685–1696.
- Klemperer, S., Hobbs, R. & British Institutions Reflection Profiling Syndicate, 1992. *The BIRPS Atlas: deep seismic reflection profiles around the British Isles*, Cambridge University Press, Cambridge, UK.
- Klingelhöfer, F., Edwards, R.A., Hobbs, R.W. & England, R.W., 2005. Crustal structure of the NE Rockall trough from wide-angle seismic data modeling, *J. geophys. Res.*, **110**(B11105), doi:10.1029/2005JB003763.
- Kodaira, S. *et al.*, 1995. Crustal structure of the Lofoten continental margin, off northern Norway, from ocean-bottom seismographic studies, *Geophys. J. Int.*, **121**, 907–924.
- Korenaga, J., Holbrook, W.S., Kent, G.M., Kelemen, P.B., Detrick, R.S., Larsen, C., Hopper, J.R. & Dahl-Jensen, T., 2000. Crustal structure of the southeast Greenland margin from joint refraction and reflection seismic tomography, *J. geophys. Res.*, **105**, 21 591–21 614.
- Korenaga, J., Kelemen, P.B. & Holbrook, W.S., 2002. Methods for resolving the origin of large igneous provinces from crustal seismology, *J. geophys. Res.*, **107**(B9), 2178–3005.
- Larsen, H. & Jakobsdóttir, S., 1988. Distribution, crustal properties and significance of seaward-dipping reflectors off east Greenland, in *Early Tertiary Volcanism and the Opening of the North-East Atlantic*, no. 39, pp. 95–114, Spec. Publ. Geol. Soc. London.
- Larsen, M., Hamberg, L., Olaussen, S. & Stemmerik, L., 1996. Cretaceous–Tertiary pre-drift sediments of the Kangerlussuaq area, southern East Greenland, *Grønlands Geologisk Undersøgelse, Bulletin*, **172**, 37–41.
- Larsen, M., Hamberg, L., Olaussen, S., Nørgaard-Pedersen, & Stemmerik, L., 1999. Basin evolution in southern East Greenland: an outcrop analog for Cretaceous–Paleogene basins on the North Atlantic volcanic margins., *AAPG Bull.*, **83**(8), 1236–1261.
- Lunnon, Z.C., Christie, P.A.F. & White, R.S., 2003. An evaluation of peak and bubble tuning in sub-basalt seismology: modelling and results, *First Break*, **21**, 51–56.
- Maresh, J. & White, R.S., 2005. Seeing through a glass, darkly: strategies for imaging through basalt, *First Break*, **23**, 27–33.
- Maresh, J., White, R.S., Hobbs, R.W. & Smallwood, J.R., 2006. Seismic attenuation of Atlantic margin basalts: observations and modeling, *Geophysics*, **71**, 211–221, doi: 10.1190/1.2335875.
- McBride, J.M., White, R.S., Smallwood, J.R. & England, R.W., 2004. Must magmatic intrusion in the lower crust produce reflectivity?, *Tectonophysics*, **388**, 271–297.
- Mudge, D.C. & Rashid, B., 1987. The geology of the Faeroe Basin area, in *Petroleum Geology of Northwest Europe*, pp. 751–763, Graham and Trotman, London.
- Pálmason, G., 1980. A continuum model of crustal generation in Iceland, *J. Geophys.*, **47**, 7–18.
- Parkin, C.J., Lunnon, Z.C., White, R.S., Christie, P.A.F. & iSIMM team, 2007. Imaging the pulsing iceland mantle plume through the Eocene, *Geology*, **35**, 93–96.
- Peate, I.U., Larsen, M. & Leshner, C.E., 2003. The transition from sedimentation to flood volcanism in the Kangerlussuaq basin, East Greenland: basaltic pyroclastic volcanism during the initial Palaeogene continental break-up, *J. Geol. Soc., Lond.*, **160**, 759–772.
- Planke, S., 1994. Geophysical response of flood basalts from analysis of wire line logs: ocean Drilling Program Site 642, Vøring volcanic margin, *J. geophys. Res.*, **99**, 9279–9296.
- Raum, T. *et al.*, 2005. Sub-basalt structures east of the Faroe Islands revealed from wide-angle seismic and gravity data, *Petrol. Geosci.*, **11**, 291–308.
- Richardson, K.R., White, R.S., England, R.W. & Fruehn, J., 1999. Crustal structure east of the Faroe Islands: mapping sub-basalt sediments using wide-angle seismic data, *Petrol. Geosci.*, **5**, 161–172.
- Shaw, F., Worthington, M.H., Andersen, M.S., Petersen, U.K. & the Seifaba Group, 2008. Seismic attenuation in Faroe Islands basalts, *Geophys. Prospect.*, **56**, 5–20, doi: 10.1111/j.1365-2478.2007.00665.x.
- Sørensen, A.B., 2003. Cenozoic basin development and stratigraphy of the Faeroes area, *Petrol. Geosci.*, **9**, 189–207.
- Spitzer, R., White, R.S. & iSIMM, Team, 2005. Advances in seismic imaging through basalts: a case study from the Faeroe–Shetland basin, *Petrol. Geoscience*, **11**, 147–156.



- Spitzer, R., White, R.S., Christie, P.A.F. & iSIMM Team, 2008. Seismic characterization of basalt flows from the Faroes margin and the Faroe-Shetland Basin, *Geophys. Prospect.*, **56**, 21–31, doi: 10.1111/j.1365-2478.2007.00666.x.
- Staples, R.K., White, R.S., Brandsdóttir, B., Menke, W., Maguire, P.K. H. & McBride, J.H., 1997. Färoe-Iceland Ridge Experiment 1. Crustal Structure of northeastern Iceland, *J. geophys. Res.*, **102**(B4), 7849–7866.
- Stoker, M.S., Hitchen, K. & Graham, C.C., 1993. United Kingdom offshore regional report: the geology of the Hebrides and West Shetland shelves, and adjacent deep-water areas, Tech. rep., HMSO, London.
- Vidale, J.E., 1990. Finite-difference calculation of traveltimes in three dimensions, *Geophysics*, **55**, 521–526.
- Vogt, U., Makris, J., O'Reilly, B.M., Hauser, F., Readman, P.W., Jacob, A.W.B. & Shannon, P.M., 1998. The Hatton Basin and continental margin: crustal structure from wide-angle seismic and gravity data, *J. geophys. Res.*, **103**(B6), 12 545–12 566.
- Voss, M. & Jokat, W., 2007. Continent–ocean transition and voluminous magmatic underplating derived from *P*-wave velocity modelling of the East Greenland continental margin, *Geophys. J. Int.*, **170**, 580–604.
- Waagstein, R., 1988. Structure, composition and age of the Faeroe basalt plateau, in *Early Tertiary Volcanism and the Opening of the NE Atlantic*, Vol. 39, pp. 225–238, eds Morton, A.C. & Parson, L.M., Geol. Soc., Lond. Spec. Pub.
- White, R. & McKenzie, D., 1989. Magmatism at Rift Zones: the generation of volcanic continental margins and flood basalts, *J. geophys. Res.*, **94**, 7685–7729.
- White, R.S. & Smith, L.K., 2009. Crustal structure of the Hatton and the conjugate east Greenland rifted volcanic continental margins, NE Atlantic, *J. geophys. Res.*, **114**, B02305, doi: 10.1029/2008JB005856.
- White, R.S., Smallwood, J.R., Flidner, M.M., Boslaugh, B., Maresh, J. & Fruehn, J., 2003. Imaging and regional distribution of basalt flows in the Faeroe-Shetland Basin, *Geophys. Prospect.*, **51**, 215–231.
- White, R., Smith, L., Roberts, A., Christie, P., Kuszniir, N. & iSIMM, Team, 2008. Lower–crustal intrusion on the North Atlantic continental margin, *Nature*, **452**(06887), 460–464, doi: 10.1038/nature06687.
- Zelt, C.A. & Barton, P.J., 1998. Three-dimensional seismic refraction tomography: a comparison of two methods applied from the Faeroe Basin, *J. geophys. Res.*, pp. 7187–7210.
- Zelt, C.A. & Smith, R.B., 1992. Seismic traveltime inversion for 2–D crustal velocity structure, *Geophys. J. Int.*, **108**, 16–34.
- Ziolkowski, A., Hanssen, P., Gatliff, R., Li, X.-Y. & Jakubowicz, H., 2001. The use of low frequencies for sub-basalt imaging, in *Proceedings of the 71st Annual International Meeting*, pp. 74–77, Society of Exploration Geophysicists.